

Tera-mode of Spatiotemporal N00N States

Xiaoqin Gao,¹ Yingwen Zhang,^{2,*} Alessio D'Errico,¹ Khabat Heshami,^{2,1} and Ebrahim Karimi^{1,2}

¹*Department of physics, University of Ottawa, Advanced Research Complex,
25 Templeton Street, K1N 6N5, Ottawa, ON, Canada*

²*National Research Council of Canada, 100 Sussex Drive, K1A 0R6, Ottawa, ON, Canada*

(Dated: August 20, 2021)

Two-photon interference is widely used in quantum information processing, e.g., state engineering and designing quantum gates, as well as in quantum sensing and metrology. This includes the generation and characterization of N00N states, which provide a phase measurement sensitivity that is beyond the shot-noise limit. There have been numerous efforts in generating N00N states with a photon number higher than 2, since their measurement sensitivity increases with N. Both photon number state and modal (temporal, spectral, and spatial) properties of light offer advantages in sensing, where the latter is achieved through mode-multiplexed measurements. Here, we experimentally demonstrate, with the aid of a recently developed photon-detection technology, measurement and characterization of up to tera-mode spatiotemporal correlations in two-photon interference and use it to generate high-dimensional two-photon N00N-states, which can be advantageous for multiphase estimation. We observe a high bi-photon interference and coalescence visibility of $\sim 64\%$ and $\sim 88\%$ for a tera (10^{12}) and 0.2 tera (2×10^{11}) spatiotemporal modes, respectively. These results open up a route for practical applications of using the spatiotemporal degrees of freedom in two-photon interference, and in particular, for quantum sensing and communication.

Whenever two identical photons enter a 50:50 beamsplitter (BS) through different input ports, they will “bunch” together – a result of bosons wanting to occupy the same quantum state – and will always exit through the same exit port [1–4]. This is known as the two-photon interference effect and was experimentally demonstrated by the Hong-Ou-Mandel (HOM) interference experiment [1]. Two-photon interference arises from the destructive interference between Feynmann paths; hence, it is purely quantum in nature [5]. HOM interferometry is nowadays widely used in quantum optics experiments and related technologies, e.g., for the characterization of photon-pair sources [6], in quantum imaging [7–10], quantum communication protocols and quantum cloning [11, 12], generation of entangled states [13, 14], and for Boson sampling [15]. The figure of merit of HOM interference is the visibility of the photon “bunching” effect, either observed as a dip in the two-photon coincidence between photons exiting from different ports of the BS, or as a peak in the two-photon coincidence between photons exiting from the same ports of the BS, referred to as coalescence. The visibility of the HOM peak/dip for a classical source cannot be higher than 50% [4, 16]. The visibility of HOM experiments is affected by all the imperfections which introduce differences between the quantum state of the two incoming photons, e.g., differences in frequency, polarization and transverse momentum. Consequently, experiments typically involve interference between two photons which are superpositions of a small number of spatial and temporal modes. This is done either by post-selection, using single-mode optical fibres in the detection stage, or by filtering the spatial modes with pinholes [17]. However, there is a strong interest in

quantum optics applications involving a large number of modes: high-dimensional states exhibit large information capacity [18], provide better security thresholds in quantum communication protocols [19], and can be useful for reducing the noise in quantum imaging [20]. Recently, HOM interference with a high number of spatiotemporal modes, i.e., a million modes ($\sim 10^6$), has been reported [21] – with a HOM dip visibility of $\sim 60\%$.

Performing HOM measurements in the spatiotemporal domain requires very long data acquisition times, which often have limited accuracy. Either physical raster scanning of detectors [22] and apertures [23] are employed, or spatially resolved EMCCD cameras are used [21]. The former technique generally provides good timing but poor spatial resolution, while the latter gives good spatial resolution but poor timing and significant noise. In this work, we make use of a new type of 3-dimensional imaging technology (TPX3CAM [24, 25]), which allows the user to surpass the trade-off between high spatial or high timing resolution in photon correlation measurements. We report the direct measurement, with a data acquisition time of only a few seconds, of up to a tera ($\sim 10^{12}$) spatiotemporal modes in HOM interference. Spatiotemporal correlation measurements are performed in the near field of the crystal with a peak and dip visibility of, respectively, $\sim 68\%$ and $\sim 62\%$. By reducing the number of measured spatiotemporal modes to $\sim 2 \times 10^{11}$ we can achieve a dip and peak visibility of $\sim 86\%$ and $\sim 94\%$, respectively. These results have been obtained exploiting the strong transverse momentum anti-correlations arising from spontaneous parametric down conversion (SPDC) [26], and the capability of TPX3CAM to post-select on a specific set of spatiotemporal modes. This allowed us to certify the generation of a multi-mode N00N state with $N = 2$. N00N states are a powerful tool for quantum supersensitivity [27] and quantum superresolution [28]

* Yingwen.Zhang@nrc-cnrc.gc.ca

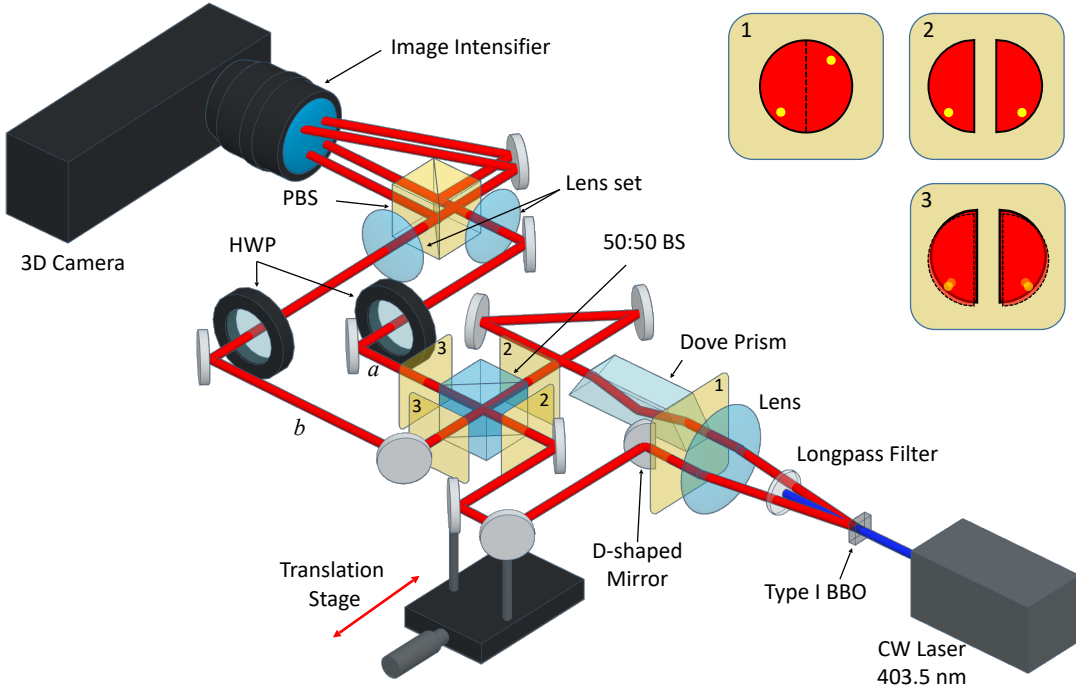


FIG. 1. **Experimental setup for imaging spatiotemporal N00N state in the near field of the BBO crystal.** A vertically polarized continuous-wave pump beam (403.5 nm, waist diameter 700 μm) induces Type-I spontaneous parametric down-conversion (SPDC) in a 0.5-mm-thick BBO crystal. A lens is used to map the SPDC state in the transverse momentum degree of freedom. Correlated photons are then split into different optical paths with a D-shaped mirror, and then interfere at a balanced beamsplitter (BS), with the outputs labelled “a” and “b”. A Dove prism and the number of mirrors map the momentum anti-correlations on the lens plane to momentum correlations at the BS output ports. A delay line constructed with the translation stage allows for adjustments of the optical paths of the two photons. For imaging the two photon N00N state in the near field, a lens set, two half-wave plates (HWPs) oriented at 22.5°, and a polarizing beamsplitter (PBS) are employed. This allows for further splitting of the two beams emerging from the 50:50 BS into four, and hence measuring constructive and destructive HOM interferences simultaneously. The insets show the beam projections which are (1) before the D-shaped mirror, (2) before the BS, and (3) after the BS, respectively.

beyond the shot noise limit or at the Heisenberg limit since they can be used to measure phases with uncertainties scaling as $O(1/N)$. Moreover, multi-mode N00N states have been identified as a candidate to perform multiple-phase estimation with improved sensitivity compared with the case of single mode N00N states [29].

Results

Multimode HOM scheme. In order to simultaneously perform HOM interference between a high number of modes, we consider the quantum state generated in Type-I SPDC. The bi-photon quantum state, in the thin crystal approximation, is given by,

$$|\Psi\rangle = \int d^2\mathbf{q} \phi(\mathbf{q}) |\mathbf{q}\rangle_s |-\mathbf{q}\rangle_i, \quad (1)$$

where $\mathbf{q} = (q_x, q_y)$ is the projection of the linear momentum on the plane transverse to the propagation direction, $\phi(\mathbf{q})$ is the bi-photon wavefunction (determined by the pump amplitude shape and the phase matching) [26], and

i and s stand for idler and signal photon, respectively. Equation (1) can be seen as a consequence of momentum conservation: any signal photon emitted with momentum \mathbf{q} is correlated with an idler photon possessing momentum $-\mathbf{q}$. Transverse momentum is mapped into transverse position, and *vice versa*, using a lens where the nonlinear crystal is kept at the lens focal plane. As illustrated in Fig. 1, correlated photons are routed into two different paths by a D-shaped mirror. In order to obtain HOM interference for each value of \mathbf{q} , the two paths of the interferometer must be designed in such a way that, at the output ports of the BS, one of the two paths has implemented the coordinates transformation $\mathbf{q} \rightarrow -\mathbf{q}$. This is obtained by means of a vertically oriented Dove prism, implementing $q_y \rightarrow -q_y$, and by a different parity in the number of reflections in the two paths (including the reflection from the BS), which corresponds to applying $q_x \rightarrow -q_x$. An alternative approach would be to exploit the transverse position correlations, which would require imaging the crystal plane on the BS (e.g., see [21]); however, the resulting visibility can be strongly affected by imaging imperfections. A detailed

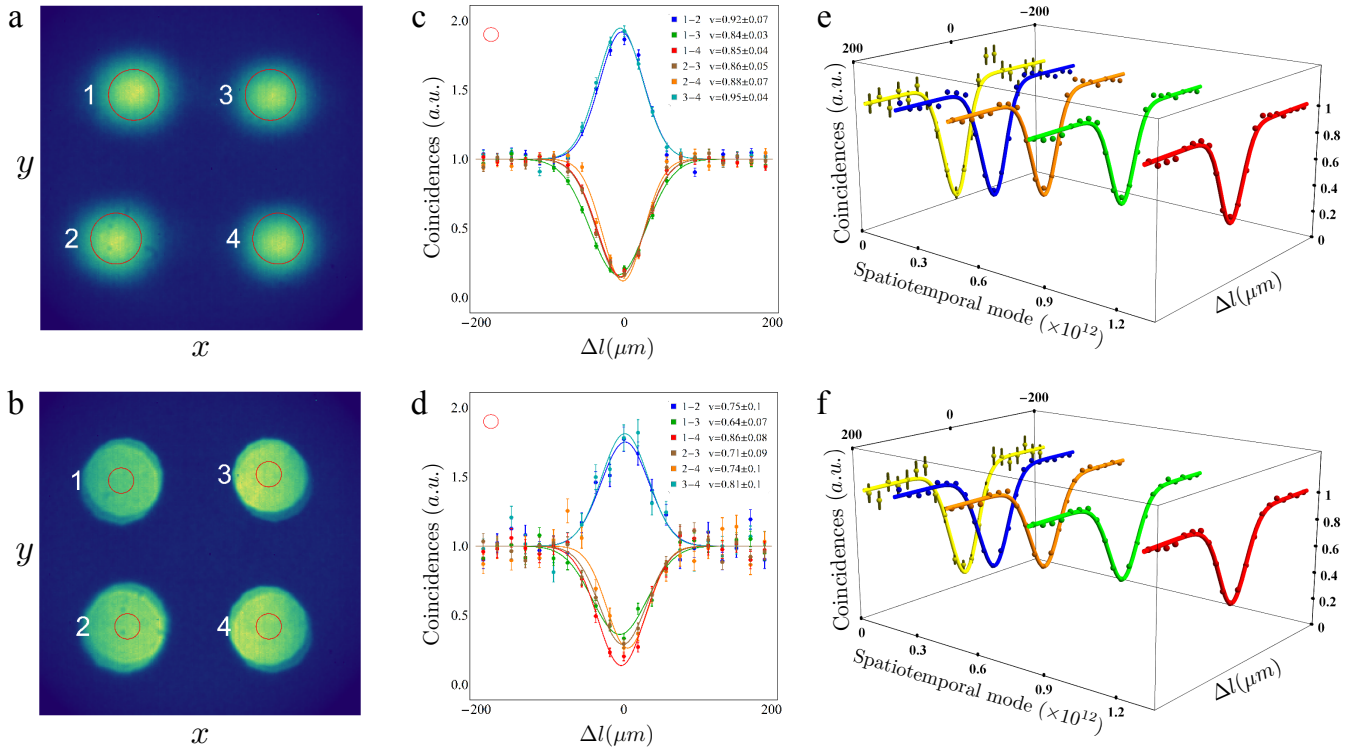


FIG. 2. Multi-mode N00N states by imaging multi-mode photon “bunching” and “anti-bunching” in both the near field and the far field of the BBO crystal. **a-b** Continuous exposure images recorded on the camera placed in, respectively, the near field and the far field. The different spots are labelled with numbers – i.e., 1, 2, 3, 4 – corresponding to different paths. **c-d** Two-fold normalized coincidences in the near (far) field with selecting 1,256 (314) spatial modes (no. of pixels within the circled region). For these spatial modes, $\sim 2.1 \times 10^{11}$ spatiotemporal modes are measured in total. The different colored data points and curves corresponds to coincidences (and corresponding Gaussian fits) between different spots (specified in the figure legend) obtained by varying the length of the two paths in the HOM interferometer. The cases 1-2 and 3-4 correspond to photon pairs exiting the same port of the interferometer; hence they give rise to HOM coalescence. All other combinations correspond to photon pairs exiting different ports of the BS, thus giving a HOM dip. **e-f** Two-fold normalized coincidences in the near (far) field with selecting different number of spatiotemporal modes. As an example, there are $\sim 5.2 \times 10^{10}$, $\sim 2.1 \times 10^{11}$, $\sim 4.7 \times 10^{11}$, $\sim 8.4 \times 10^{11}$, and $\sim 1.3 \times 10^{12}$ spatiotemporal modes respectively selected between the beam spot 2-4 (1-4). The corresponding visibilities of the HOM dip are 0.92 ± 0.10 (0.86 ± 0.08), 0.88 ± 0.07 (0.75 ± 0.04), 0.78 ± 0.06 (0.65 ± 0.03), 0.70 ± 0.05 (0.61 ± 0.02), and 0.64 ± 0.05 (0.60 ± 0.02) respectively. Some error bars are not visible, being smaller than the symbols.

experimental setup is shown in Fig. 1. Two-photon interference is obtained at the output of a 50:50 BS. The two optical paths corresponding to the BS’s output ports are further split into two, allowing for the measurement of both photon bunching and anti-bunching. The four resulting beams are finally imaged onto the 3D camera.

When perfect multi-mode HOM interference is registered, the resulting state, in the photon number basis, is a multi-mode two-photon N00N state, i.e.,

$$|\psi\rangle = \mathcal{N} \sum_{k=1}^M (|2_{k,a}, 0_{k,b}\rangle + |0_{k,a}, 2_{k,b}\rangle) \otimes |\text{vacuum}'\rangle. \quad (2)$$

Here, \mathcal{N} is a normalization factor, k is the mode index, M is the total number of modes, a/b are the BS output ports indices, and $|\text{vacuum}'\rangle$ represents vacuum state for all other modes $k' \neq k$. The choice of the spatial mode set

depends on the actual application that one may consider. In imaging experiments, k can be chosen as corresponding to the camera’s pixel position. Therefore, it depends on the imaging system and can be associated with an area of the transverse position or transverse momentum space. This choice is not arbitrary since one can always devise a protocol in which pixel degrees of freedom are consistently mapped into spatial ones.

The probability (and consequently the fidelity) of generating a N00N state is given by the visibility of the HOM interference measured by tuning the optical path difference in the interferometer. Visibilities of the coalescence peak in photon bunching (an increase of coincidence counts detecting photons coming from the same output port) and of the HOM dip in photon anti-bunching (a decrease of coincidence counts detecting photons coming from different output port) are defined as $V_{\text{peak}} =$

$(C_{max} - C_{\infty})/C_{\infty}$ and $\mathcal{V}_{\text{dip}} = (C_{\infty} - C_{min})/C_{\infty}$, where C_{max} and C_{min} are the maximum and minimum coincidence count rates at the peak and dip, respectively. C_{∞} is the coincidence count rate when the difference in the two photon paths length is large and outside the dip/peak.

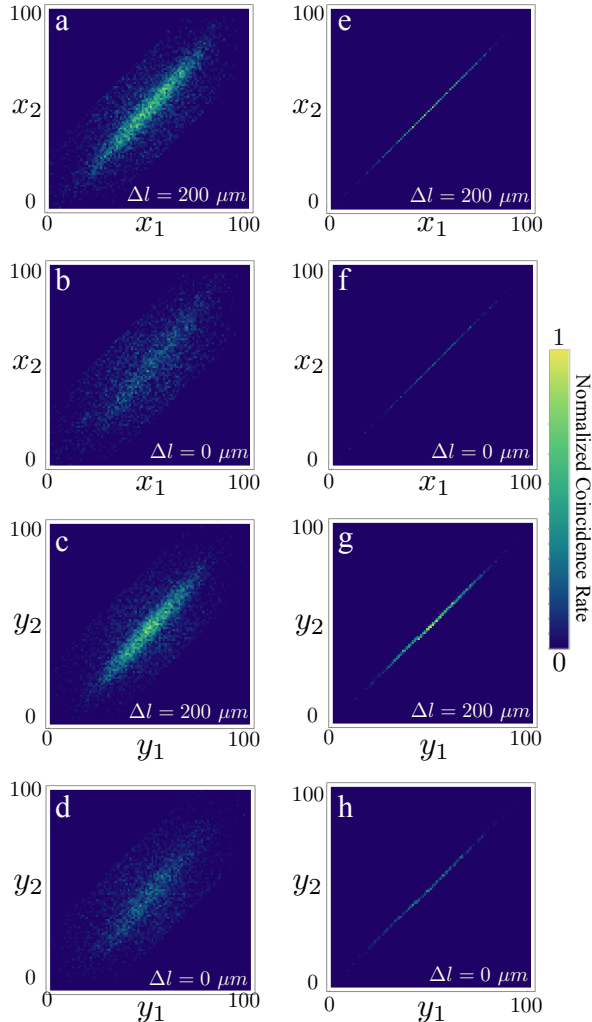


FIG. 3. Measured near field spatial correlations. Through post-processing, the 3D camera allows one to filter out the counts from a given region in the correlation space. By selecting only diagonal correlations (panels **e-h**, corresponding to a 1 pixel wide window) one can remove residual background noise and effectively post-select on the entangled state of Eq. (1). We show the correlations in the x and y coordinate components imaged outside and inside the HOM dip position (corresponding to $\Delta l = 0 \mu\text{m}$). The post-selection procedure can contribute to increasing the HOM visibility. Indeed, with a 30 pixel wide spatial correlation selection band (panels **a-d**) and a 1 pixel wide selection band between the spots 1-3 in Fig. 2 **a**, we have, respectively, $\mathcal{V} = 0.59 \pm 0.03$ and $\mathcal{V} = 0.67 \pm 0.04$.

Multi-mode N00N states. In order to preliminarily align the setup, we first coupled photons from the BS output ports to multi-mode optical fibres, with a core diam-

eter of $(50 \pm 1) \mu\text{m}$, connected to single-photon avalanche detectors in order to search for the HOM dip, reaching a visibility 0.78 ± 0.02 . The non-perfect visibility may be due to various system imperfections, and in particular, the alignment of the optics (mirrors and BS and Dove prism orientation). The BS output modes (labelled *a* and *b*) are each split in two before being sent on the TPX3CAM camera sensor. With reference to Fig. 2 **a**, the spots 1-2 and 3-4 come from, respectively, the output ports *a* and *b*. Hence, coincidences between either 1 and 2, or 3 and 4 show coalescence peaks when scanning the optical path delay (Δl), while all the other combinations give HOM dips. The results are shown in Fig. 2 **c**. We measured total coincidences selecting circular areas around each spot with radius equal to 20 pixels (Fig. 2 **c**) and obtaining average visibilities of $\sim 88\%$. The visibility increases when selecting circular areas around each spot with larger radius, as shown in Fig. 2 **e**. A visibility of $\sim 64\%$ for a HOM dip between spot 2-4 can be obtained if the radius is equal to 50 pixels. We also report in the Supplementary Materials a similar analysis of the influence of the selected regions on the visibility for a HOM peak.

Using a different set of imaging lenses in the experimental setup, the same analysis was performed with the camera placed in the crystal's far field. The total coincidences selecting circular areas in Fig. 2 **b** around each spot are measured with radius equal to 10 pixels (Fig. 2 **d**). The resulting visibilities are, on average, $\sim 75\%$. The decrease in visibility for a larger selected region, as shown in Fig. 2 **f**, is likely due to imperfections in the alignment of optics and the fact that the Dove prism is cutting part of the SPDC beam, causing a broadening of the correlations on the BS plane for the higher momentum modes, which lowers the visibility. For example, there are $\sim 1.3 \times 10^{12}$ spatiotemporal modes by selecting 7,850 spatial modes for a 50 pixels radius, and obtaining a visibility $\sim 0.60 \pm 0.02$ for a HOM dip between the spot 1-4. Thus a wider window includes a larger number of modes affected by the setup imperfections.

As a next step, we examined how the HOM interference affects the spatial correlations. Figure 3 **a-d** show the joint probability distribution of the spatial correlations in both the horizontal and vertical directions. We measured the joint probability distributions in two different scenarios: outside the HOM dip (Fig. 3 **a** and **c**), and inside the HOM dip (Fig. 3 **b** and **d**). The state generated in the latter scenario is a N00N state. Due to the wide spatial correlation bands, which can be caused by a variety of factors such as crystal thickness, HOM interferometer alignment and a displaced imaging plane, the number of non-overlapping spatial modes is only ~ 100 . However, through post-selection with a stricter spatial correlation condition (at the cost of losing coincidence events), as shown in Fig. 3 **e-h**, we can boost the number of spatial modes to ~ 7850 ($\pi \times 50 \times 50$). Consequently, this also reduces the background noise and improves the HOM dip visibility by $\sim 10\%$. The visibility of bi-photon interfer-

ence, and consequently the N00N states, depends on the indistinguishability of the photons at the BS. Placing an iris with a variable aperture just after the BBO crystal allows one to control and improve the HOM visibility further. With the effective camera temporal resolution of 6 ns (limited by the signal rise time of the scintillator in the image intensifier [30]), and with the restraint that only a single camera is used, we can obtain a total of between $\sim 10^{11}$ to $\sim 10^{12}$ spatiotemporal modes. It is possible to increase the spatiotemporal modes by another order of magnitude by employing two cameras for each mode a and b where simultaneous spatiotemporal correlation measurements are performed between the cameras. Note that we have also performed the same analysis with the camera placed in the crystal's far-field. The obtained results are similar to the near-field and are shown in the Supplementary Materials.

Discussion

From the experimental data we can determine the Schmidt number for our setup, i.e. the effective number of modes if all modes have the same detection probability. The Schmidt number for a particular degree of freedom can be determined using [31, 32].

$$K = \frac{1}{\sum_i P_i^2}, \quad (3)$$

where P_i is the detection probability for mode i and must be normalized to unity, i.e. $\sum_i P_i = 1$.

As the photon detection probability in each pixel for the near field spatial degrees of freedom (DOF) is proportional to the pump beam profile, we can use one of the beam spots captured in Fig. 2 a to determine the Schmidt number for the spatial DOF, K_s . Thus, from equation (3) we obtain an average of $K_s = 3.23 \times 10^3$ from the four beam spots in Fig. 2 a. For the temporal DOF, since a continuous-wave pump laser is used, the probability of detecting a photon is the same at all times (ignoring laser power fluctuations) with a probability of 6×10^{-9} , which is just the timing resolution for our camera. Thus, the Schmidt number for the temporal modes is simply $K_t = 1/(6 \times 10^{-9}) = 1.68 \times 10^8$. The total Schmidt number for all measured spatiotemporal modes is then $K = K_s \times K_t = 5.38 \times 10^{11}$. As shown in the section of Methods, multimode N00N states can be advantageous in multiple phase estimation experiments even in the case of limited visibility. The latter introduces an increase of $1/\mathcal{V}$ of the total variance of the estimators $|\Delta\theta|^2$, which can be compensated by an increase of repeated measurements. Its effect is thus equivalent to losses in the system.

Two-photon interference has been previously investigated with spatial modes, e.g., Hermite-Gauss modes [17, 33], Laguerre-Gauss modes [34, 35], and position and momentum modes [21, 23]. In these approaches, each spatial mode is scanned individually, or the spatial modes

are measured simultaneously but with a poor timing resolution. Moreover, these techniques require very long data acquisition times. Here, we have demonstrated simultaneous measurements of spatial and temporal correlations in HOM interference with high resolution and high speed. In addition, the generated states after the two-photon interference, i.e., N00N state with $N = 2$, were analyzed for up to 10^{12} spatiotemporal modes, demonstrating a high-dimensional N00N state with an average fidelity of 64%. By reducing the number of spatiotemporal modes to 2×10^{11} , a fidelity of 88% can be achieved. We point out that the same kind of setup can be employed for generating N00N states with $N > 2$, however certify the generation in our experiment of this state would have required a brighter SPDC source.

Our ability to swiftly measure a large number of spatiotemporal modes in HOM interference can be exploited in many applications, such as a source for high-dimensional two-photon N00N states, which can be used in sensing applications [36], increasing quantum repeater dimensionality with the inclusion of position/momentum modes, and quantum imaging applications such as in optical coherence tomography.

Methods

Multiple phase estimation with non-perfect N00N states. Multimode N00N states are close to optimal states for estimating multiple parameters with a low variance [29]. Indeed, as shown in Ref. [29], a multimode-N00N state would allow to estimate d different and independent phases with an uncertainty:

$$|\Delta\theta|^2 = \frac{d(d+1)}{2N^2}, \quad (4)$$

where N is the number of photons and $d+1$ is the number of modes carried by the quantum state (one mode needs to be used as a reference). Here, following [29], we use $d+1$ instead of M to label the total number of modes since the relation between d and M depends on the actual measurement scheme -see below for examples. This uncertainty has a better scaling as a function of d compared to the repeated use of single-mode N00N states (where $|\Delta\theta|^2 = \frac{d^3}{2N^2}$). For comparison, a classical strategy would give a total variance $|\Delta\theta|^2 = \frac{d^2}{N}$.

Here, we address the problem of evaluating the uncertainty $|\Delta\theta|^2$ for the case in which the actual state is of the kind,

$$|\Psi\rangle = \sqrt{\mathcal{V}}|N00N\rangle + e^{i\phi}\sqrt{1-\mathcal{V}}|N00N^\perp\rangle, \quad (5)$$

where ϕ is an arbitrary relative phase. Hence, we take in account for the possibility of an imperfect generation of the N00N state. The multimode N00N can be expressed

as:

$$|N00N\rangle = \frac{1}{\sqrt{d+1}} (|N, 0, \dots, 0\rangle + \dots + |0, \dots, 0, N\rangle). \quad (6)$$

It is easy to see that the state in Eq. (2) can be rewritten in this way with the appropriate labelling of modes, which may depend on the phase estimation setup that one would devise. For instance, if the output port label is added to the M spatio-temporal modes we would have $d+1 = 2M$. Otherwise, if one couples, say, the path "a" to a single mode fiber, then that path can be associated with the reference mode and $d = M$. The $|N00N^\perp\rangle$ state contains a superposition of all the configuration in which there are photons exiting from both the output ports of the beam splitter. For the 2-photon case, this can be written as:

$$|N00N^\perp\rangle = \sqrt{\frac{2}{(d+1)d}} (|1, 1, 0, \dots, 0\rangle + |1, 0, 1, \dots, 0\rangle + \dots + |0, \dots, 1, 1\rangle). \quad (7)$$

For our purposes, it is important to note that the normalization factor of $|N00N^\perp\rangle$ will be at least of the order $1/d$ (and will decrease for $d \gg N > 2$).

Following Humpreys *et al* (2013) [29], we use the following notation for an arbitrary multimode N -photon state:

$$|\psi_N^{(d)}\rangle = \sum_{i=1}^D a_i |N_{i,1}, N_{i,2}, \dots, N_{i,d+1}\rangle, \quad (8)$$

where $\sum_i N_{i,k} = N$ and $D = (N+d)!/N!d!$. In our case, from Eq. (5) we have:

$$a_i = \begin{cases} \sqrt{\frac{\mathcal{V}}{d+1}} & 1 \leq i \leq d+1 \\ e^{i\phi} \sqrt{1-\mathcal{V}} \beta & i > d+1 \end{cases}, \quad (9)$$

with $\beta = \sqrt{2/[d(d+1)]}$ for $N = 2$ (for $d \gg N > 2$,

$\beta \sim O(1/d)$, and

$$N_{i,l} = \begin{cases} N\delta_{i,l} & 1 \leq i \leq d+1 \\ \tilde{\delta} & i > d+1 \end{cases}, \quad (10)$$

where $\tilde{\delta}$ is a finite superposition of Kronecker's deltas labelling the modes in which one or more photons are present.

For the multiple phase estimation, the variance of the estimators will be lower bounded by the trace of the inverse Fisher information matrix, i.e.,

$$|\Delta\theta|^2 \geq \text{Tr}[F_\theta^{-1}] \quad (11)$$

where F_θ was calculated in Ref. [29] to be

$$[F_\theta]_{l,m} = 4 \sum_{i=1}^D N_{i,l} N_{i,m} |a_i|^2 - 4 \sum_{i,j=1}^D N_{i,l} N_{j,m} |a_i|^2 |a_j|^2 \quad (12)$$

In our case:

$$[F_\theta]_{l,m} = 4 \left[\frac{\mathcal{V}N^2}{d+1} \delta_{l,m} + O(1/d^2) \right]. \quad (13)$$

Since we are interested in the case of high d ($d \sim 10^{11-12}$ and $d \gg N$), we can keep the first term, and obtain

$$|\Delta\theta|^2 \approx \frac{d(d+1)}{4\mathcal{V}N^2}. \quad (14)$$

Data availability

The authors declare that the data supporting the findings of this study are available within the paper and its Supplementary Materials file.

REFERENCES

- [1] C. K. Hong, Z. Y. Ou, and L. Mandel, "Measurement of subpicosecond time intervals between two photons by interference," *Phys. Rev. Lett.* **59**, 2044–2046 (1987).
- [2] H. Fearn and R. Loudon, "Theory of two-photon interference," *J. Opt. Soc. Am. B* **6**, 917–927 (1989).
- [3] Rarity J G and Tapster P R, "Photons and quantum fluctuations," (CRC Press, 1988) Chap. Nonclassical Effects in Parametric Downconversion, p. 122.
- [4] Frédéric Bouchard, Alicia Sit, Yingwen Zhang, Robert Fickler, Filippo M Miatto, Yuan Yao, Fabio Sciarrino, and Ebrahim Karimi, "Two-photon interference: the hong-ou-mandel effect," *Reports on Progress in Physics* **84**, 012402 (2021).
- [5] TB Pittman, DV Strekalov, Alan Migdall, MH Rubin, AV Sergienko, and YH Shih, "Can two-photon interference be considered the interference of two photons?" *Physical Review Letters* **77**, 1917 (1996).
- [6] Francesco Graffitti, Jérémie Kelly-Massicotte, Alessandro Fedrizzi, and Agata M Brańczyk, "Design considerations for high-purity heralded single-photon sources," *Physical Review A* **98**, 053811 (2018).
- [7] Magued B Nasr, Bahaa EA Saleh, Alexander V Sergienko, and Malvin C Teich, "Demonstration of dispersion-canceled quantum-optical coherence tomography," *Physical review letters* **91**, 083601 (2003).
- [8] Malvin Carl Teich, Bahaa EA Saleh, Franco NC Wong, and Jeffrey H Shapiro, "Variations on the theme of quantum optical coherence tomography: a review," *Quantum*

Information Processing **11**, 903–923 (2012).

[9] Jie Tang, Yang Ming, Wei Hu, and Yan-qing Lu, “Spiral holographic imaging through quantum interference,” *Applied Physics Letters* **111**, 011105 (2017).

[10] Zeferino Ibarra-Borja, Carlos Sevilla-Gutiérrez, Roberto Ramírez-Alarcón, Hector Cruz-Ramírez, and Alfred B U’Ren, “Experimental demonstration of full-field quantum optical coherence tomography,” *Photonics Research* **8**, 51–56 (2020).

[11] Eleonora Nagali, Linda Sansoni, Fabio Sciarrino, Francesco De Martini, Lorenzo Marrucci, Bruno Piccirillo, Ebrahim Karimi, and Enrico Santamato, “Optimal quantum cloning of orbital angular momentum photon qubits through hong-ou-mandel coalescence,” *Nature Photonics* **3**, 720–723 (2009).

[12] Frédéric Bouchard, Robert Fickler, Robert W. Boyd, and Ebrahim Karimi, “High-dimensional quantum cloning and applications to quantum hacking,” *Science Advances* **3**, e1601915 (2017).

[13] Yoon-Ho Kim, Sergei P Kulik, Maria V Chekhova, Warren P Grice, and Yanhua Shih, “Experimental entanglement concentration and universal bell-state synthesizer,” *Physical Review A* **67**, 010301 (2003).

[14] Manuel Erhard, Mehul Malik, Mario Krenn, and Anton Zeilinger, “Experimental greenberger–horne–zeilinger entanglement beyond qubits,” *Nature Photonics* **12**, 759–764 (2018).

[15] Max Tillmann, Borivoje Dakić, René Heilmann, Stefan Nolte, Alexander Szameit, and Philip Walther, “Experimental boson sampling,” *Nature photonics* **7**, 540–544 (2013).

[16] Rainer Kaltenbaek, Bibiane Blauensteiner, Marek Źukowski, Markus Aspelmeyer, and Anton Zeilinger, “Experimental interference of independent photons,” *Phys. Rev. Lett.* **96**, 240502 (2006).

[17] S. P. Walborn, A. N. de Oliveira, S. Pádua, and C. H. Monken, “Multimode hong-ou-mandel interference,” *Phys. Rev. Lett.* **90**, 143601 (2003).

[18] Manuel Erhard, Mario Krenn, and Anton Zeilinger, “Advances in high-dimensional quantum entanglement,” *Nature Reviews Physics* **2**, 365–381 (2020).

[19] Nicolas J Cerf, Mohamed Bourennane, Anders Karlsson, and Nicolas Gisin, “Security of quantum key distribution using d-level systems,” *Physical review letters* **88**, 127902 (2002).

[20] Giorgio Brida, Marco Genovese, Alice Meda, and Ivano Ruo Berchera, “Experimental quantum imaging exploiting multimode spatial correlation of twin beams,” *Physical Review A* **83**, 033811 (2011).

[21] Fabrice Devaux, Alexis Mosset, Paul-Antoine Moreau, and Eric Lantz, “Imaging spatiotemporal hong-ou-mandel interference of biphoton states of extremely high schmidt number,” *Phys. Rev. X* **10**, 031031 (2020).

[22] Gur Lubin, Ron Tenne, Ivan Michel Antolovic, Edoardo Charbon, Claudio Bruschini, and Dan Oron, “Quantum correlation measurement with single photon avalanche diode arrays,” *Opt. Express* **27**, 32863–32882 (2019).

[23] P. S. K. Lee and M. P. van Exter, “Spatial labeling in a two-photon interferometer,” *Phys. Rev. A* **73**, 063827 (2006).

[24] <https://www.amsclins.com/tpx3cam/>.

[25] A. Nomerotski, “Imaging and time stamping of photons with nanosecond resolution in Timepix based optical cameras,” *Nuclear Instruments and Methods in Physics Research Section A: Accelerators, Spectrometers, Detectors and Associated Equipment* **937**, 26–30 (2019).

[26] Stephen P Walborn, CH Monken, S Pádua, and PH Souto Ribeiro, “Spatial correlations in parametric down-conversion,” *Physics Reports* **495**, 87–139 (2010).

[27] Yonatan Israel, Shamir Rosen, and Yaron Silberberg, “Supersensitive polarization microscopy using noon states of light,” *Phys. Rev. Lett.* **112**, 103604 (2014).

[28] Lee A. Rozema, James D. Bateman, Dylan H. Mahler, Ryo Okamoto, Amir Feizpour, Alex Hayat, and Aephraim M. Steinberg, “Scalable spatial superresolution using entangled photons,” *Phys. Rev. Lett.* **112**, 223602 (2014).

[29] Peter C. Humphreys, Marco Barbieri, Animesh Datta, and Ian A. Walmsley, “Quantum enhanced multiple phase estimation,” *Phys. Rev. Lett.* **111**, 070403 (2013).

[30] Ianzano Christopher, Svihra Peter, Flament Mael, Hardy Andrew, Cui Guodong, Nomerotski Andrei, and Figueroa Eden, “Fast camera spatial characterization of photonic polarization entanglement,” *Scientific Reports* **10**, 6181 (2020).

[31] C. K. Law, and J. H. Eberly, “Analysis and Interpretation of High Transverse Entanglement in Optical Parametric Down Conversion,” *Phys. Rev. Lett.* **92**, 127903 (2004).

[32] F. M. Miatto, H. Di Lorenzo Pires, S. M. Barnett, and M. P. van Exter, “Spatial Schmidt modes generated in parametric down-conversion,” *The European Physical Journal D* **66**, 263 (2012).

[33] Yingwen Zhang, Shashi Prabhakar, Carmelo Rosales-Guzmán, Filippus S. Roux, Ebrahim Karimi, and Andrew Forbes, “Hong-ou-mandel interference of entangled hermite-gauss modes,” *Phys. Rev. A* **94**, 033855 (2016).

[34] Ebrahim Karimi, Daniel Giovannini, Eliot Bolduc, Nicolas Bent, Filippo M. Miatto, Miles J. Padgett, and Robert W. Boyd, “Exploring the quantum nature of the radial degree of freedom of a photon via hong-ou-mandel interference,” *Phys. Rev. A* **89**, 013829 (2014).

[35] Yingwen Zhang, Filippus S. Roux, Thomas Konrad, Megan Agnew, Jonathan Leach, and Andrew Forbes, “Engineering two-photon high-dimensional states through quantum interference,” *Science Advances* **2**, e1501165 (2016).

[36] Markus Hiekkämäki, Frédéric Bouchard, and Robert Fickler, “Photonic angular super-resolution using twisted n0n states,” [arXiv:2106.09273 \[quant-ph\]](https://arxiv.org/abs/2106.09273).

Acknowledgments

The authors would like to thank Aephraim Steinberg, Frédéric Bouchard, Dilip Paneru and Alicia Sit for valuable discussions, and Manuel F Ferrer-Garcia for the great help with figures, and Mohammadreza Rezaee for the great help in the laboratory management. This work was supported by the Canada Research Chairs (CRC), the High Throughput and Secure Networks (HTSN) Challenge Program at the National Research Council of Canada, Canada First Research Excellence Fund (CFREF) Program, and Joint Centre for Extreme Photonics (JCEP).

Author contributions

X.G., Y.Z., and A.D. designed and carried out the exper-

iment with the help of E.K.. X.G., A.D., Y.Z., K.H., and E.K. analysed the results. X.G., A.D., and Y.Z. wrote the manuscript with input from all authors. Y.Z., K.H., and E.K. supervised the project.

Competing interests

The authors declare no competing interests.

Additional Information Supplementary Materials accompanies this article.

SUPPLEMENTARY MATERIAL
TERA-MODE OF SPATIOTEMPORAL NOON STATES

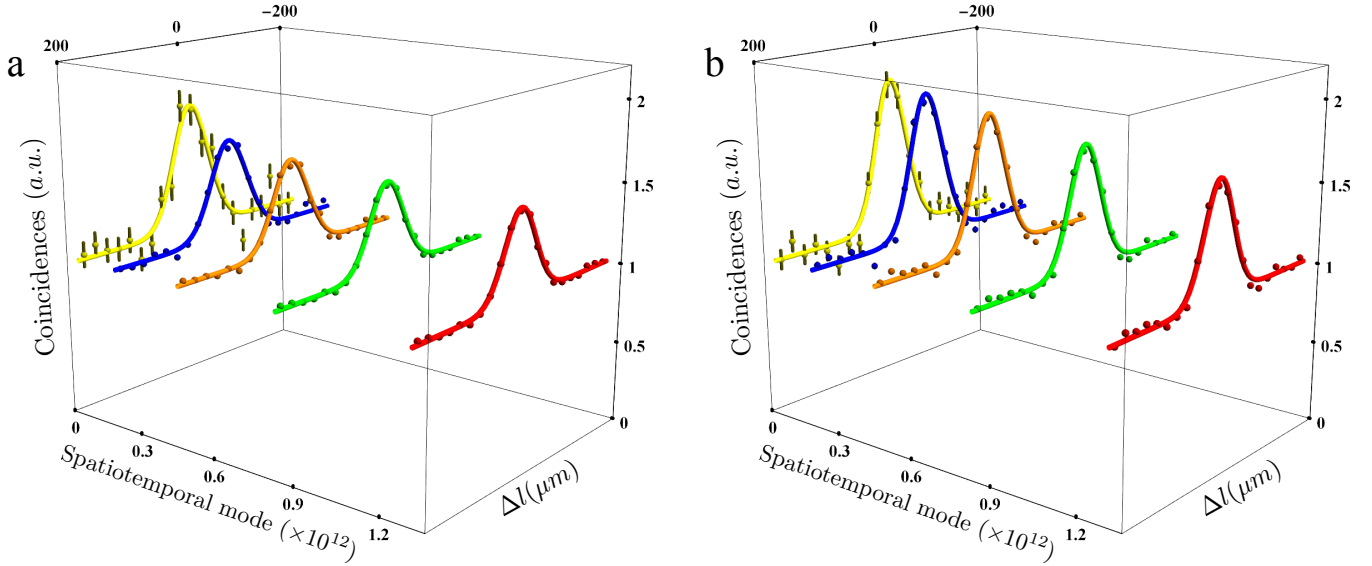


FIG. 4. **Visibilities for the HOM peak in the far field and the near field with selecting $\sim 5.2 \times 10^{10}$, $\sim 2.1 \times 10^{11}$, $\sim 4.7 \times 10^{11}$, $\sim 8.4 \times 10^{11}$, and $\sim 1.3 \times 10^{12}$ spatiotemporal modes respectively.** **a** Multi-mode HOM interference between the spot 3-4 in the far field. The related visibilities for HOM peak are 0.81 ± 0.10 , 0.62 ± 0.04 , 0.57 ± 0.04 , 0.54 ± 0.02 , and 0.53 ± 0.02 respectively. **b** Multi-mode HOM interference between the spot 1-2 in the near field. The related visibilities for HOM peak are 0.97 ± 0.10 , 0.92 ± 0.07 , 0.85 ± 0.05 , 0.76 ± 0.05 , and 0.69 ± 0.05 respectively. Some error bars are not visible, being smaller than the symbols.

Fig. 4 shows the influence of the selected region radius on the visibility for a HOM peak in both the far field (Fig. 4 a) and the near field (Fig. 4 b).

Thanks to its ability to measure spatiotemporally resolved coincidences, the TPX3Cam technology allows to directly reconstruct the position correlations of the measured state. As a consequence one can select regions of interest in the correlation space, which allows reducing the background and to post-select on a desired quantum state. In Fig. 5 we illustrate how one can post-select on the state given in the main text (which manifests perfect momentum anti-correlations, associated with perfect position correlations) within the precision given by the pixel area. Fig. 5 a-d show the measured correlations (for path delays corresponding to inside and outside the HOM interference) when selecting a circular region of 50 pixels radius and considering counts within a 10 pixels wide stripe in the correlation space. In Fig. 5 e-h the stripe is reduced to a width of 1 pixel. In the case shown this amounts to an increase of the visibility of $\sim 10\%$.

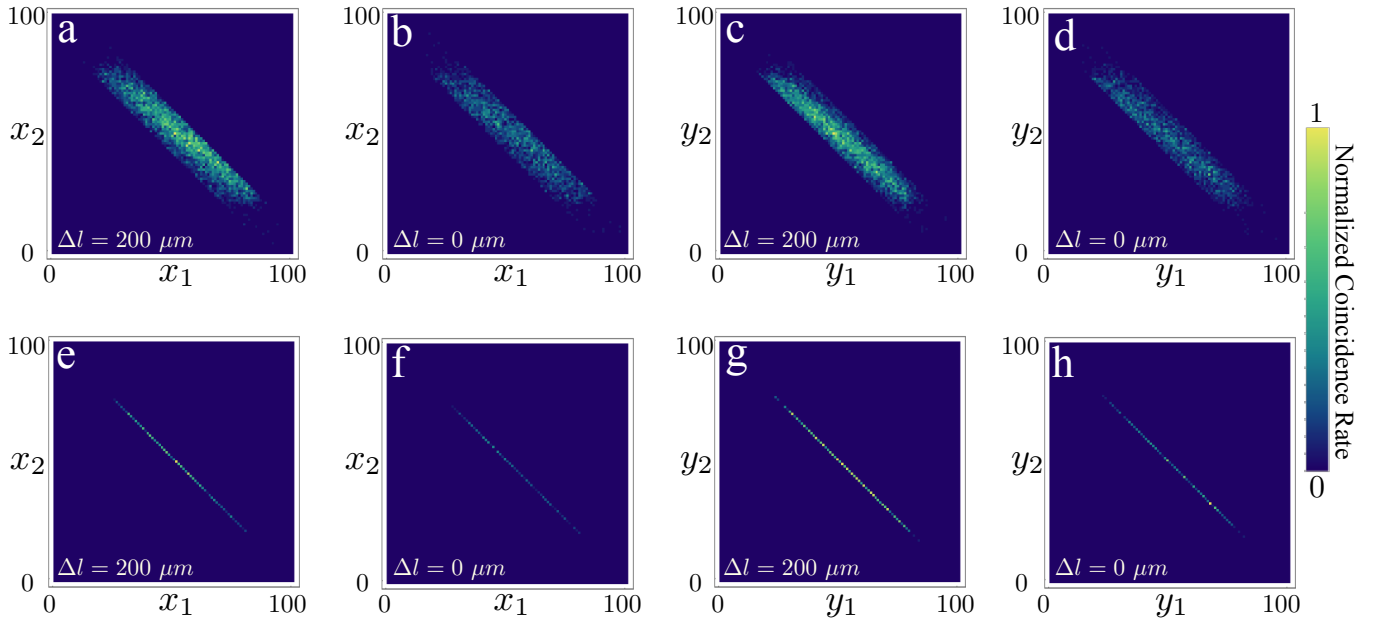


FIG. 5. **Detected spatial correlations in the far field.** One can reduce background by selecting only diagonal correlations (panels **e-h**, corresponding to a 1 pixel wide window). The correlations in the x and y coordinate components imaged outside and inside the HOM dip position (corresponding to $\Delta l = 0 \mu\text{m}$). We have for the 10 pixels (panels **a-d**) and 1 pixel selection band (panels **e-h**), respectively, $\mathcal{V} = 0.51 \pm 0.03$ and $\mathcal{V} = 0.56 \pm 0.06$.